Magnetic and microwave absorbing properties of low-temperature sintered BaZr$_x$Fe$_{(12-x)}$O$_{19}$

Li Deng, [ab] Yang Zhao, [ab] Zhaoming Xie, [*ab] Zuohua Liu, [ab] Changyuan Tao [ab] and Rongrui Deng [ab]

In the present work, to enhance the reflection loss and change the magnetic resonance frequency of barium ferrite sintered at low temperature, different amounts of Zr ion were introduced to BaFe$_{12}$O$_{19}$ to substitute the Fe ion. A series of M-type barium hexaferrite samples having the nominal composition BaZr$_x$Fe$_{(12-x)}$O$_{19}$ (x = 0.0, 0.3, 0.6, 0.9 and 1.2) was successfully synthesized by heat treatment at a relatively low temperature (900 °C) for 2 h. In order to study the phases, morphologies and magnetic properties of the substituted barium ferrites, X-ray diffraction (XRD), scanning electron microscopy (SEM) and vibrating sample magnetometry (VSM) were used. The XRD patterns indicated that all samples were single phase M-type ferrites. The SEM images showed that all samples were hexagonal-shaped particles and the average size was about 500 nm. Simultaneously, a potassium chloride additive can effectively reduce the sintering temperature of barium ferrites and their formation and morphology are apparently not affected. The VSM results demonstrated that the coercivity steeply decreased from 4772.43 Oe to 797.34 Oe when the Zr ion substitution amount increased from 0.0 to 1.2 but the saturation magnetization remained almost constant (M_s = 49.71–63.06 emu g^{-1}). Furthermore, the complex electromagnetic parameters were collected by a vector network analyzer (VNA) and the microwave absorbing properties were calculated according to transmission theory. It was found that the reflection loss is enhanced with increasing x. The minimum reflection loss value of −30.2 dB at 16.75 GHz was observed and the bandwidth is about 2.46 GHz for the x = 1.2 sample. BaZr$_x$Fe$_{(12-x)}$O$_{19}$ might be a promising candidate for applications of LTCC (low-temperature co-fired ceramic) substrates for millimeter wave circulators and filters.

1. Introduction

With the rapid development of communication technology and the electronic industry, problems of electromagnetic pollution (EMP) and electromagnetic interference (EMI) are becoming increasingly serious.[1–3] In recent years, the research on electromagnetic wave absorbers with the capability of absorbing unwanted electromagnetic signals has become a hot spot. Ferrites with excellent magnetic and dielectric properties are regarded as the best magnetic material for electromagnetic wave absorbers. Compared to the ferrites that possess spinel and garnet structures, barium ferrites (BaFe$_{12}$O$_{19}$, often denoted as BaM) with a hexagonal magnetoplumbite structure are considered to be a promising absorbing material owing to their large magnetocrystalline anisotropy (K_1 = 3.3 × 10^5 J m^{-3}),[4] high saturation magnetization (M_s = 72 emu g^{-1}), high coercivity (H_c = 6700 Oe),[5] excellent chemical stability and high frequency application.

At present, there are several common methods for synthesizing barium ferrite, such as the dynamic hydrothermal method,[6] co-precipitation method,[7] high-energy ball milling method,[8] sol–gel method[9] and so on. However, in order to form the crystalline structure of barium ferrite, the sintering temperature of these methods is usually higher than 1200 °C,[10] which limits the application of barium ferrite in low temperature co-fired ceramic (LTCC) technology. LTCC technology is an important technology to realize the miniaturization and integration of portable communication devices (such as mobile phones) and wave absorbing devices (such as filters). In the process of LTCC fabrication, magnetic or dielectric materials and a silver electrode material are co-fired at low temperature (<961 °C),[11] so it is necessary for materials sintered at low temperature to achieve their specific structure and properties. Therefore, for the purpose of reducing the sintering temperature, the addition of low melting-point materials has been tried. In our study, KCl with a melting point of 770 °C is selected as an additive to reduce the calcining temperature of ferrite.

For the pure barium ferrite, according to a report, the resonance frequency is too high (42.5 GHz),[12] the minimum of reflection loss is larger than −5 dB and the microwave absorbing property is poor. Ion substitution has been

*a*Chongqing Key Laboratory of Chemical Process for Clean Energy and Resource Utilization, Chongqing University, Chongqing 400044, China. E-mail: xiezm@cqu.edu.cn

*b*College of Chemistry and Chemical Engineering, Chongqing University, Chongqing 400044, China

considered to be the most efficient method to improve the properties of barium ferrite among various techniques. Currently, two methods of ionic substitution have been reported. One is to substitute Ba^{2+} [13–15] with other cations, and the other is the substitution of Fe^{3+}.[16–18] The saturation magnetization, coercive force, magnetic resonance frequency and magnetocrystalline anisotropy field were altered when other ions were introduced into the barium ferrite structure. However, so far, there has been no report on Zr-doped $BaFe_{12}O_{19}$ nanoparticles sintered at low temperature. So, the effect of Zr substitution at different levels on barium ferrite sintered at low temperature was studied.

In the present study, $BaZr_xFe_{(12-x)}O_{19}$ (x = 0.0, 0.3, 0.6, 0.9 and 1.2) ferrite powders were prepared with the co-precipitation method and sintered with potassium chloride as an additive at 900 °C. Subsequently, the impacts of doping Zr^{4+} on the phases, morphologies and magnetic properties of the samples were discussed. Finally, the complex permeability, permittivity and absorbing properties were discussed.

2. Experimental

$BaZr_xFe_{(12-x)}O_{19}$ particles with different nominal compositions (x = 0.0, 0.3, 0.6, 0.9 and 1.2) were synthesized by a modified flux method, which consists of two processes, one is chemical co-precipitation, the other is synthesis from a salt melt.[19] An aqueous solution containing the metal salts $BaCl_2 \cdot 2H_2O$ (AR), $FeCl_3 \cdot 6H_2O$ (AR) and $ZrO(NO_3)_2 \cdot 6H_2O$ (AR) in the proportions needed for the ferrite was dropped into an aqueous solution of Na_2CO_3 (AR). Subsequently, a high concentration of Na_2CO_3 was added to adjust the pH of the mixing solution to 9 and the solution was heated at 70 °C for 2 h. The reacted solution was filtered, washed thoroughly and dried. Then, the as-prepared precursors were mixed with KCl (AR) and heated at 900 °C for 2 h in air. Ferrite grains crystallized from the KCl molten salt. After the KCl was dissolved in water, $BaZr_xFe_{(12-x)}O_{19}$ particles were obtained.

X-ray diffraction (XRD) with Cu Kα radiation was employed to identify the crystalline phases of the final product. The micrographs and the chemical composition of the ferrites were recorded using scanning electron microscopy (SEM) and energy dispersive X-ray (EDX) analysis. The magnetic properties of the samples were measured by vibrating sample magnetometry (VSM, Lake Shore 735). The complex permittivity and complex permeability of the ferrites in the frequency range of 2–18 GHz were measured directly with a vector network analyzer (VNA, N5244A).

3. Results and discussion

3.1. X-ray diffraction (XRD) analysis

The XRD patterns of the $BaZr_xFe_{(12-x)}O_{19}$ nanoparticles with nominal compositions (x = 0.0, 0.3, 0.6, 0.9, 1.2) obtained at 900 °C are shown in Fig. 1. Fig. 1(a) shows that all peaks belong to the $BaFe_{12}O_{19}$ phase; no other phase is apparently detectable. The pure phase M-type barium ferrites were successfully synthesized under low temperature sintering by adding the KCl

additive. Furthermore, the peak positions are obviously changed and the relative intensities alter slightly as the substitution value x increases. As Fe^{3+} ions were increasingly substituted by Zr^{4+} ions, the diffraction angles of the strongest three peaks (110), (107) and (114) were observed to decrease (shown in Fig. 1(b)). The result indicates that the crystal lattice expanded with the increase of Zr content. Table 1 displays the specific lattice parameters. It is obvious that lattice parameters "a" and "c" increase slightly, while "c" increases faster, as shown in Fig. 2. This suggests that the c-axis undergoes more expansion than the a-axis because of ion substitution. Furthermore, cell volume increases as x increases. This may be due to the fact that the ion radius of Zr^{4+} (0.072 nm) is larger than that of Fe^{3+} (0.067 nm). It has been reported that the structure type of ferrite may be quantified by the lattice parameter ratio. When the "c/a" ratio is lower than 3.98, the ferrite is considered to be in the form of an M-type hexaferrite structure.[20] In this work, the "c/a" ratio varies from 3.9372 to 3.9432. This demonstrated that the obtained samples are of M-type hexagonal ferrite structure.

Fig. 1(b) also shows that upon increasing the substitution amount x, the relative intensities of the peaks in the XRD patterns decreased and the peaks broadened, implying that the grains became smaller and the crystallinity decreased. The average crystallite size (D_{hkl}) of different $BaZr_xFe_{(12-x)}O_{19}$ nanoparticles was calculated according to Scherrer's equation. The results are summarized in Table 1. The crystallite sizes decrease from 58.7 nm (x = 0.0) to 52.6 nm (x = 1.2) for $BaZr_xFe_{(12-x)}O_{19}$ with increasing Zr^{4+} substitution content. This may be attributed to the fact that the radius of Zr^{4+} is slightly different from that of Fe^{3+}, so the substitution will cause the lattice to distort and the internal stress caused by lattice distortion will impede the growth of grains but the crystal structure will not be influenced.[21] The relatively small size of the grains may also be attributed to the restriction of grain growth by liquid phase formation, which agrees with some reports in the literature.[22]

3.2. Morphology analysis

The SEM images of Zr-doped barium ferrites calcined at 900 °C for 2 h are shown in Fig. 3. The SEM images of the samples showed that well-formed hexagonal grains were present and the agglomeration of particles hardly occurred. The size of particles for all samples was less than 1 μm; most of them were about 500 nm. In the process of sintering, the KCl additive not only has little impact on the morphology of the nanoparticles but also plays an important role in reducing the calcining temperature.[22] The hexagonal shape of the samples gradually became irregular as Zr concentration increased and the sizes increased slightly. This might be due to the fact that the ferrite formation reaction was promoted by the Zr^{4+} ion, which is in agreement with other research.[23] It is clear that some small particles appeared as Zr was introduced. Furthermore, the number of small particles increased with x content.

Energy dispersive X-ray (EDX) analysis was carried out in order to confirm the chemical composition of $BaZr_xFe_{(12-x)}O_{19}$ sintered at 900 °C for 2 h. Fig. 4 shows the typical EDX spectra

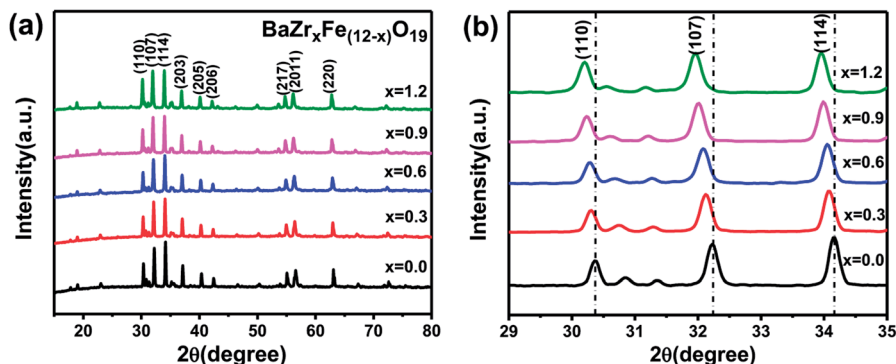**Fig. 1** (a) XRD patterns of BaZr$_x$Fe$_{(12-x)}$O$_{19}$ (0.0 ≤ x ≤ 1.2) nanoparticles calcined at 900 °C for 2 h; (b) partially enlarged XRD patterns of (a).

Table 1 Variation in XRD cell parameters and crystallite sizes of BaZr$_x$Fe$_{(12-x)}$O$_{19}$ with dopant (Zr)

x	a (Å)	c (Å)	c/a	Cell volume (Å³)	Crystallite size (nm)
0.0	5.8650	23.0990	3.9384	688.09	58.7
0.3	5.8760	23.1700	3.9432	692.80	58.3
0.6	5.8760	23.1700	3.9432	692.80	54.0
0.9	5.8920	23.1980	3.9372	697.42	53.1
1.2	5.8945	23.2150	3.9384	698.52	52.6

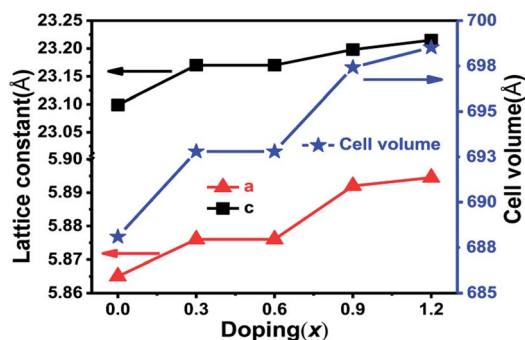**Fig. 2** Variation in lattice constants and cell volumes as a function of doping (x = Zr) in BaZr$_x$Fe$_{(12-x)}$O$_{19}$.

and the inset table is the analysis data. It was observed that all samples contain Fe, Ba and O elements, and when the x value increases, the content of Zr increases, which is consistent with the designed composition.

3.3. Magnetic measurements

Zr^{4+} substitution does not greatly influence the morphology of the nanoparticles but it does have a significant effect on the magnetic properties. As shown in Fig. 5(a), the room temperature magnetic hysteresis loops of Zr-doped ferrites sintered at 900 °C suggest that the samples possess high coercivity. The changes of the saturation magnetization (M_s) and coercivity (H_c) values of BaZr$_x$Fe$_{(12-x)}$O$_{19}$ are also displayed in Fig. 5(b). Table 2 summarizes the derived magnetic parameters. Magnetism in

ferrites is derived from the magnetic moments of ions in spin up and spin down orientations in the sublattice according to ferromagnetic theory.[24] In general, the distribution of iron ions in the crystallographic lattice determines the magnetic properties of the M-type hexaferrite to some extent. Fe^{3+} ions occupy five distinct crystallographic sites: three octahedral sites, 12k (spin up), 4f2 (spin down), and 2a (spin up), a tetrahedral site, 4f1 (spin down), and a bipyramidal site, 2b (spin up), in the structure of pure BaM.[25] Mössbauer studies demonstrated that the molar proportion of Fe^{3+} ions at different sites is Fe(12k) : Fe(4f1) : Fe(4f2) : Fe(2a) : Fe(2b) = 6 : 2 : 2 : 1 : 1 for undoped BaM.[26] The magnetic moment of barium ferrite can be inferred from the algebraic sum of iron magnetic moments at diverse sites: $M = M(12k + 2a + 2b)\uparrow - M(4f1 + 4f2)\downarrow$.[27] For pure BaFe$_{12}O_{19}$, the total magnetic moment is equal to 20 μB as the magnetic moment of Fe^{3+} is 5 μB.

As shown in Fig. 5(b) and Table 2, the obtained barium ferrite series has a high level of magnetic characteristics. With increasing x, the value of M_s first decreases to 51.41 emu g^{-1} at x = 0.3 and then increases, reaching 59.77 emu g^{-1} at x = 0.9; when x = 1.2, M_s reduces to the minimum value of 49.71 emu g^{-1}. Although there are some changes, M_s tends to be reasonably constant (M_s = 49.71–63.06 emu g^{-1}). The theoretical value of M_s for single phase BaM is 72 emu g^{-1}, as reported in the literature.[5] In this study, the maximum value of M_s is lower than the theoretical value by 12%, and this phenomenon may be influenced by the method of preparation.

It is known that magnetic properties are chiefly influenced by the occupied position of doping ions in different lattice sites of Fe^{3+} and their magnetic nature. The first decrease of M_s may be due to the fact that the dopant is substituted at the parallel 2b site at x = 0.3 and that the magnetic moment of the doped ion (Zr^{4+} = 0 μB) is smaller than that of Fe^{3+} (5 μB). When x increased from 0.3 to 0.9, the increase of M_s can be attributed to the enhancement of the total magnetic moment, which is due to Zr^{4+} ions locating at the anti-parallel 4f1 site. As x continues to increase, more Fe^{3+} (high spin) ions are converted to Fe^{2+} (low spin) by substitution of Fe^{3+} with Zr^{4+} ions, resulting in magnetic dilution occurring. Thus, the Fe^{3+}–O–Fe^{3+} super-exchange interaction is disrupted and weakened by Fe^{2+} ions and spin canting.[28] Hence, spin canting and the magnetic
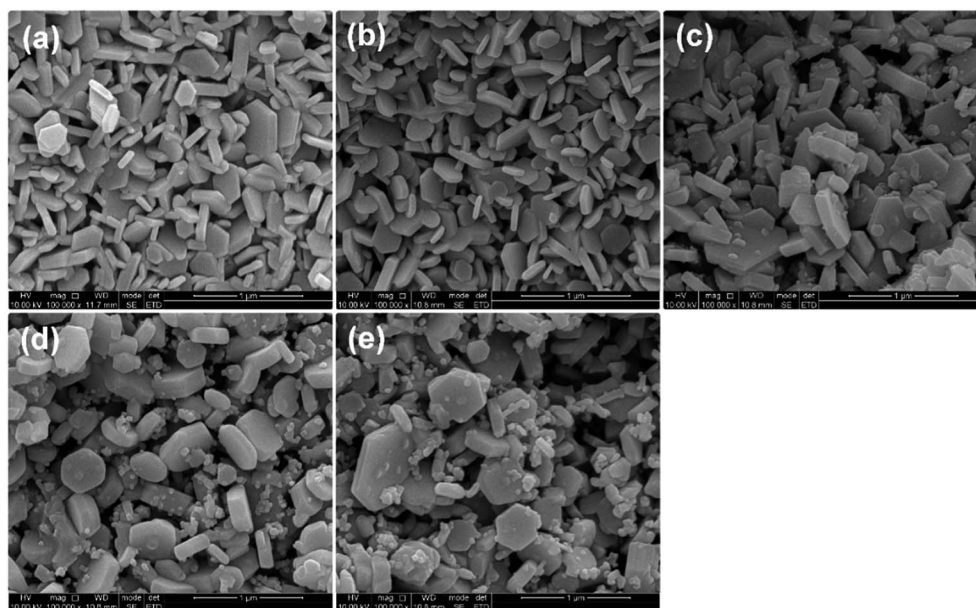
Fig. 3 SEM images of $BaZr_xFe_{(12-x)}O_{19}$ sintered at 900 °C for 2 h with KCl: (a) $x = 0.0$; (b) $x = 0.3$; (c) $x = 0.6$; (d) $x = 0.9$; (e) $x = 1.2$.

dilution effect may be two dominant reasons why $BaZr_{1.2}$-$Fe_{10.8}O_{19}$ possesses a lower M_s value.

Meanwhile, Fig. 5(b) shows that there is a relatively wide coercivity range when the substitution amount x increased from 0.0 to 1.2. It can be seen that the H_c values of the $BaZr_x$-$Fe_{(12-x)}O_{19}$ nanoparticles decrease gradually from 4772.43 Oe to 797.34 Oe as Zr substitution increases (as shown in Table 2). The theoretical value of H_c is 6700 Oe for BaM, as reported in literature.[5] The value of the coercive force in our study is reduced by 29% compared to the theoretical value, which may be affected by synthetic methods. The fall in coercivity is due partially to the larger particle sizes. As found in the SEM study
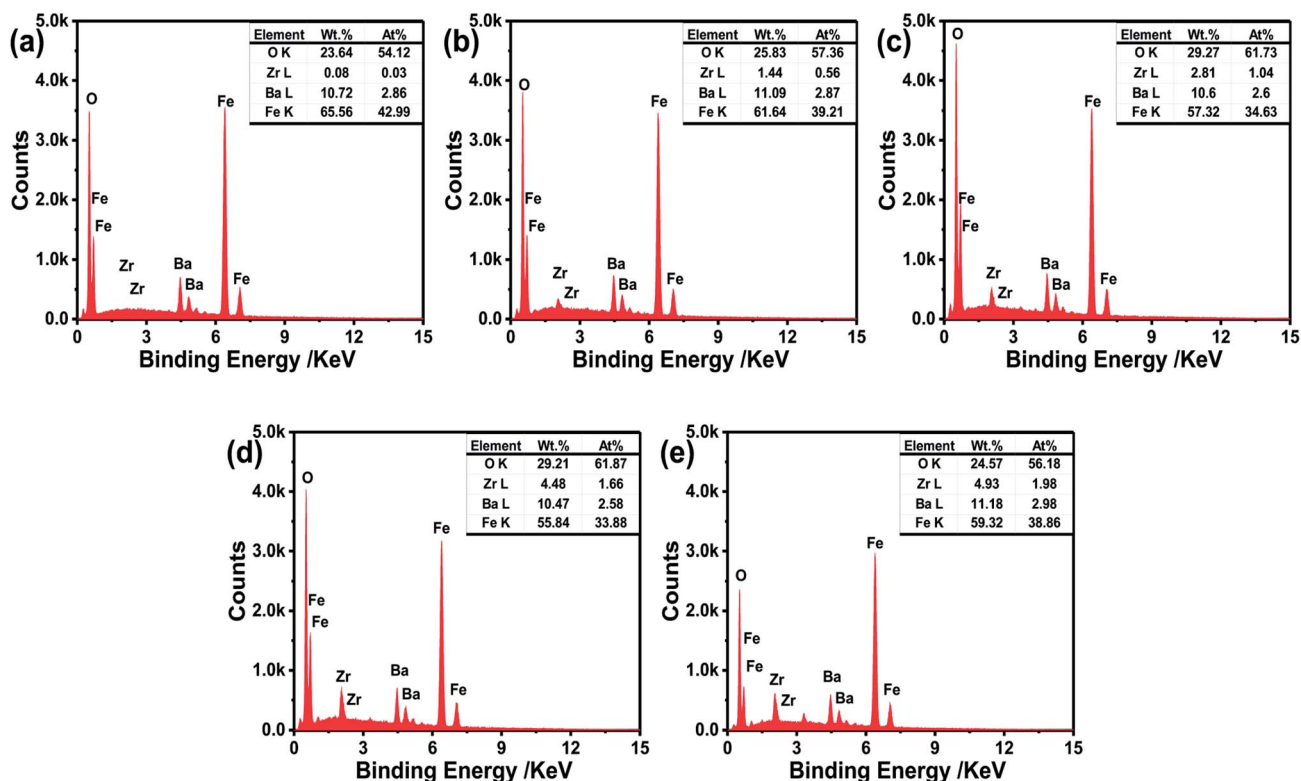

Fig. 4 EDX images of $BaZr_xFe_{(12-x)}O_{19}$ sintered at 900 °C for 2 h with KCl: (a) $x = 0.0$; (b) $x = 0.3$; (c) $x = 0.6$; (d) $x = 0.9$; (e) $x = 1.2$.

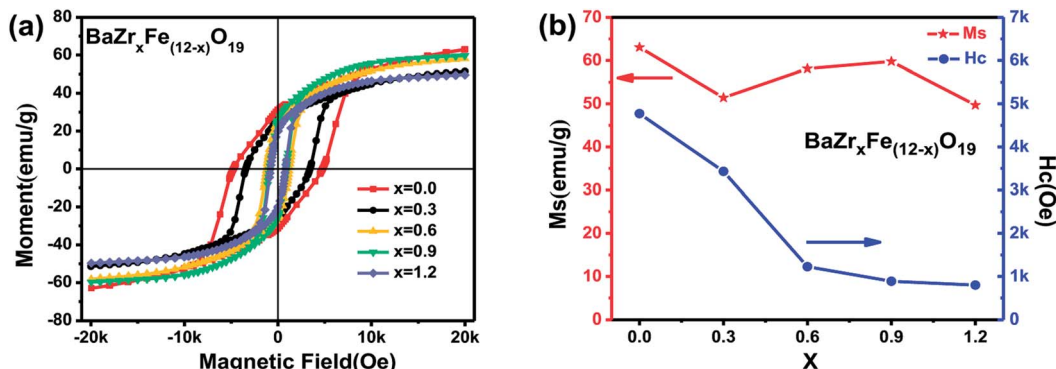**Fig. 5** (a) Hysteresis loops for the $BaZr_xFe_{(12-x)}O_{19}$ nanoparticles calcined at 900 °C for 2 h; (b) effect of x on values of M_s and H_c of $BaZr_x$-$Fe_{(12-x)}O_{19}$ nanoparticles calcined at 900 °C for 2 h.

Table 2 Magnetization data of the $BaZr_xFe_{(12-x)}O_{19}$ series synthesized by the co-precipitation method

Sample (x)	M_s (emu g^{-1})	H_c (Oe)	M_r (emu g^{-1})	M_r/M_s
$x = 0.0$	63.06	4772.43	31.24	0.50
$x = 0.3$	51.41	3431.29	25.80	0.50
$x = 0.6$	58.13	1225.88	25.73	0.44
$x = 0.9$	59.77	887.46	25.48	0.43
$x = 1.2$	49.71	797.34	20.00	0.40

(Fig. 3), the particle size of barium ferrite increased as x increased, but this fact cannot alone interpret the decline of H_c in the Zr doped samples. The other reason may be due to the fact that a reduction of the magnetocrystalline anisotropy field results from the substitution of nonmagnetic Zr^{4+} ions. As is well known, the contributions of a single Fe^{3+} ion in each position to the anisotropy constant K_1 can be sorted as -0.18, 0.18, 0.23, 0.51 and 1.4, respectively, for 12k, 4f1, 2a, 4f2 and 2b.[29] We already know that Zr^{4+} ions locate on the 2b site at low doping levels, which leads to a large decrease of H_c. And as x increases, Zr^{4+} ions gradually prefer to occupy the 4f1 site, which results in a slight decline of H_c.

3.4. Microwave characteristics

3.4.1 Complex permittivity and permeability spectra of the nanoparticles. We investigated the complex permittivity ($\varepsilon = \varepsilon' - j\varepsilon''$) and complex permeability ($\mu = \mu' - j\mu''$) of $BaZr_x$-$Fe_{(12-x)}O_{19}$ nanoparticles at varied x values ($x = 0.0, 0.3, 0.6, 0.9, 1.2$) to uncover the internal reasons for the microwave absorption properties. The variation of the real (ε') and imaginary (ε'') parts of complex permittivity for $BaZr_xFe_{(12-x)}O_{19}$ ($x = 0.0, 0.3, 0.6, 0.9, 1.2$) over the frequency range of 2–18 GHz is shown in Fig. 6(a) and (b). The ε' of complex permittivity increases from 5.33 to 5.91 with increasing frequency for the undoped sample and the ε'' is almost invariable. It was found that the value of ε' for all of the samples with Zr ion doping is larger than that of the undoped sample. The value of the imaginary part (ε'') for $x = 0.9$ increases obviously over the whole frequency range compared to the undoped sample, while the other three samples show a similar behaviour. The complex permittivity of

hexaferrites originates from intrinsic electric dipole polarization, electronic polarization, ionic polarization and interfacial polarization according to dielectric physics.[30,31] The change of the permittivity with frequency is bound up with interfacial polarization and intrinsic electric dipole polarization.[32] For the Zr substituted ferrites, the increase in ε' and ε'' may be due to the replacement of Fe^{3+} with Zr^{4+}, which results in converting some of the Fe^{3+} ions to Fe^{2+} ions to maintain charge neutrality. The electron hopping between Fe^{3+} and Fe^{2+} enhances the dielectric loss, and the excess Fe^{2+} strengthens the interfacial polarization in the Zr doped ferrites.[33]

The variation of the real (μ') and imaginary (μ'') parts of complex permeability for $BaZr_xFe_{(12-x)}O_{19}$ ($x = 0.0, 0.3, 0.6, 0.9, 1.2$) over the frequency range of 2–18 GHz is shown in Fig. 7(a) and (b). The μ' of complex permeability declines from 1.13 to 1.00 as the frequency increases for the undoped sample while the μ'' spectrum has a peak value at around 13.16 GHz. For all doped samples, the values of the real part (μ') of complex permeability are larger than that of the undoped sample and remain nearly constant. Furthermore, the value of the imaginary part (μ'') for the $x = 1.2$ sample is larger than that of the undoped sample from 2 to 18 GHz and its maximum value is about 0.19 at 18 GHz, which implies that doping Zr^{4+} can enhance the magnetic loss.

3.4.2 Microwave absorption properties of the nanoparticles. Reflection loss (RL) can be calculated from the complex permittivity (ε', ε'') and permeability (μ', μ'') with a given absorber thickness (d) by the following equations according to transmission line theory:[34]

$$RL = 20 \times \log\left|\frac{Z_{in} - Z_0}{Z_{in} + Z_0}\right| \tag{1}$$

$$Z_{in} = Z_0 \times \sqrt{\frac{\mu_r}{\varepsilon_r}} \times \tanh\left[j \times \frac{2\pi df}{c} \times \sqrt{\mu_r \varepsilon_r}\right] \tag{2}$$

where Z_{in} is the input impedance of the absorber, Z_0 is the impedance of free space, ε_r and μ_r are the complex relative permittivity and permeability of the sample, respectively, d is the thickness of the absorber layer, c is the velocity of light in a vacuum, and f is the frequency of the incident electromagnetic wave (EW). There are two basic conditions that must be met to
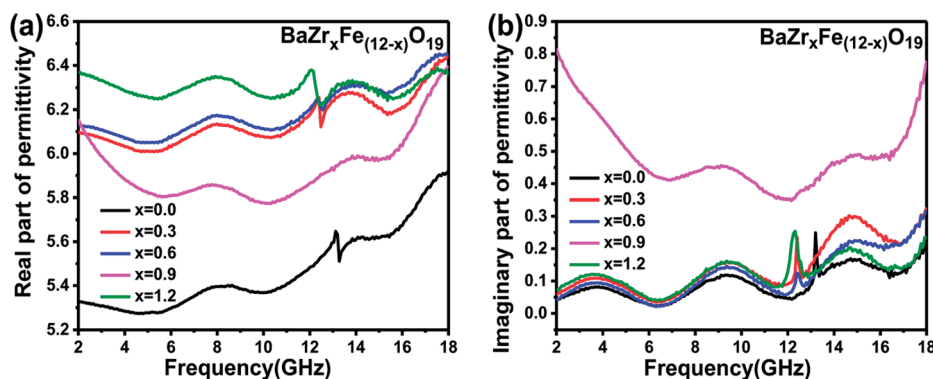
Fig. 6 Permittivity response of $BaZr_xFe_{(12−x)}O_{19}$ ferrite samples: (a) real part and (b) imaginary part.

attain excellent absorbing properties according to the literature.[35,36] One is that the electromagnetic wave can enter into absorbing materials to the utmost degree, the other is that the electromagnetic wave entering into the materials can be almost entirely attenuated.

For the purpose of finding the appropriate thickness, the reflection losses with different thicknesses were calculated based on the equations for all samples. The calculations were executed for $d = 2, 3, 4$, and 5 mm. Fig. 8 shows the reflection loss of the $BaZr_{1.2}Fe_{10.8}O_{19}$ samples at various thicknesses.

As can be seen from the figure, the absorbing property is poor and the minimum of reflection loss is larger than −10 dB from 2 to 18 GHz when the thickness is less than 4 mm. Furthermore, when the matching thickness increases to 5 mm, the minimum of the reflection loss of the $BaZr_{1.2}Fe_{10.8}O_{19}$ nanoparticles reduces to as low as −30.2 dB at 16.75 GHz; all other samples were found to have a similar nature.

Fig. 9 shows the change of the reflection loss with frequency for the $BaZr_xFe_{(12−x)}O_{19}$ nanoparticles ($x = 0.0, 0.3, 0.6, 0.9$ and 1.2) at the thickness of 5 mm. The bandwidth refers to a range of frequency where the reflection loss is lower than −10 dB. 90% of the microwaves can be absorbed in this frequency bandwidth. An excellent microwave absorbing material should possess not only a low reflection loss but also a wide frequency bandwidth. There is no obvious absorption for the samples with $x ≤ 0.3$. But, when the amount of doping is greater than 0.3, the

reflection loss and the bandwidth increase obviously and the resonance frequency slightly moves toward a lower frequency. When $x = 0.9$, the strongest reflection loss is −25.1 dB at 16.79 GHz and the bandwidth is 2.15 GHz. The reason for the improvement of reflection loss of $BaZr_{0.9}Fe_{11.1}O_{19}$ might be that the value of ε'' for $x = 0.9$ is largest among all samples (shown in Fig. 6(b)), which indicates that more incident electromagnetic wave will be attenuated via dielectric loss. As compared to the other samples, the ferrite with the composition of $BaZr_{1.2}Fe_{10.8}O_{19}$ shows the strongest microwave absorption. The minimum value of the reflection loss of the $BaZr_{1.2}Fe_{10.8}O_{19}$ nanoparticles is about −30.2 dB at 16.75 GHz and the bandwidth is about 2.46 GHz, which implies that the $BaZr_{1.2}Fe_{10.8}O_{19}$ nanoparticles possess excellent microwave absorption properties. This might be due to the fact that the value of μ'' for $x = 1.2$ is larger than that of the other four samples (shown in Fig. 7(b)), which indicates that more incident electromagnetic wave will be attenuated via magnetic loss. According to our investigation, the absorbing property of $BaFe_{12}O_{19}$ is weak and the minimum of reflection loss is larger than −5 dB. The doped barium ferrites show relatively excellent absorption properties with respect to the pure barium ferrite.

The enhancement of microwave absorption properties of the Zr ion substituted samples might be attributed to two reasons: first, the crystallite size contraction caused by the slight difference of radius between Zr^{4+} and Fe^{3+} (shown in Table 1) can
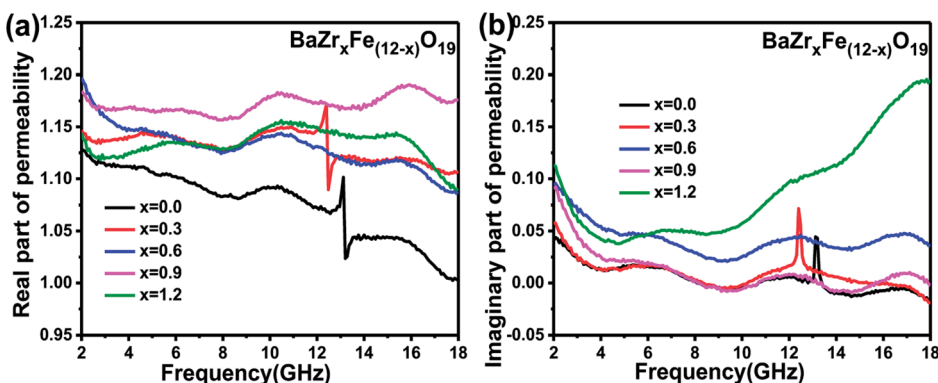

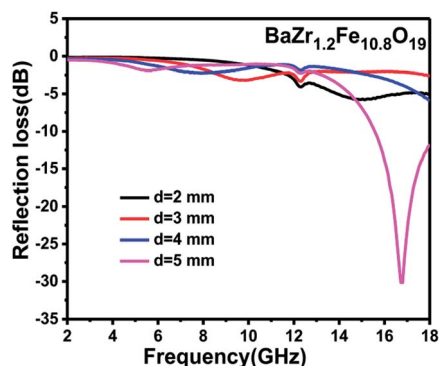**Fig. 7** Permeability response of $BaZr_xFe_{(12−x)}O_{19}$ ferrite samples: (a) real part and (b) imaginary part.

Fig. 8 The reflection loss of $BaZr_{1.2}Fe_{10.8}O_{19}$ for the thickness of $d = 2$, 3, 4, and 5 mm.

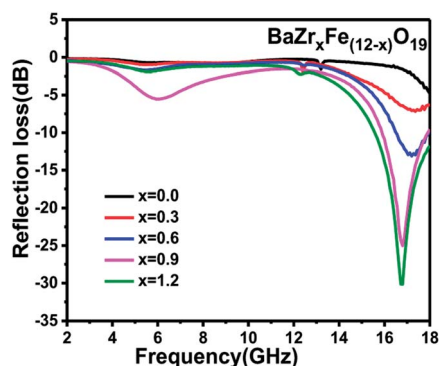**Fig. 9** The reflection loss of $BaZr_xFe_{(12-x)}O_{19}$ ferrite samples with $x =$ 0.0, 0.3, 0.6, 0.9, 1.2.

cause the surface state and grain surface energy level to vary obviously.[37] The increased interface polarization and multiple reflection will cause more energy to be absorbed when the electromagnetic wave diffuses in the materials.[38] Second, the substitution of Zr^{4+} for Fe^{3+} would result in converting some Fe^{3+} to Fe^{2+} in the ferrite structure to maintain charge neutrality. The electrons hopping between ions with different valence induces electric dipole polarization[39] and thence the dielectric loss can be enhanced after Zr doping.

4.   Conclusions

$BaZr_xFe_{(12-x)}O_{19}$ ($0 \leq x \leq 1.2$) powders with potassium chloride as an additive were successfully synthesized by a sintering route at relatively low temperature (900 °C). The XRD patterns indicated that all samples were single phase M-type ferrites. SEM images revealed that all samples are small hexagonal-shaped particles and the particle sizes are about 500 nm. The obtained samples exhibit a high level of saturation magnetization but the coercivity is continuously reduced from 4772.43 Oe to 797.34 Oe when the Zr ion substitution amount increases from 0.0 to 1.2. The dominant reason for the variations of magnetic properties is that non-magnetic Zr^{4+} ions prefer to occupy 2b sites at a low substitution level, while they occupy 4f1 sites at a high doping level. The microwave absorbing properties of

barium ferrite are greatly improved by doping Zr ions, especially $BaZr_{1.2}Fe_{10.8}O_{19}$. The minimum of the reflection loss of the $BaZr_{1.2}Fe_{10.8}O_{19}$ nanoparticles is about −30.2 dB at a matching frequency of 16.75 GHz and the bandwidth is about 2.46 GHz, which indicates that the $BaZr_{1.2}Fe_{10.8}O_{19}$ nanoparticles possess excellent microwave absorption properties. The enhancement of microwave absorption properties of the Zr ion doped ferrite samples might be attributed to the fact that the reflection loss can be enhanced by the grain size shrinkage and electrons hopping between ions with different valence induced by substitution of Fe^{3+} with Zr^{4+} ions. $BaZr_xFe_{(12-x)}O_{19}$ nanoparticles might be a good candidate for applications of LTCC substrates for millimeter wave circulators and filters.

Conflicts of interest

There are no conflicts to declare.

Acknowledgements

References

1 A. Ghasemi, A. Hossienpour, A. Morisako, A. Saatchi and M. Salehi, *J. Magn. Magn. Mater.*, 2006, **302**, 429–435.

2 B. Dai, X. Shao, Y. Ren, G. Wang, C. Pei and Y. Ma, *Mater. Lett.*, 2012, **82**, 188–190.

3 Y. Ren, S. Li, B. Dai and X. Huang, *Appl. Surf. Sci.*, 2014, **311**, 1–4.

4 V. G. Harris, Z. Chen, Y. Chen, S. Yoon, T. Sakai, A. Gieler, A. Yang, Y. He, K. S. Ziemer, N. X. Sun and C. Vittoria, *J. Appl. Phys.*, 2006, **99**, 08M911.

5 S. K. Chawla, R. K. Mudsainiyan, S. S. Meena and S. M. Yusuf, *J. Magn. Magn. Mater.*, 2014, **350**, 23–29.

6 T. Ben Ghzaiel, W. Dhaoui, A. Pasko and F. Mazaleyrat, *J. Alloys Compd.*, 2016, **671**, 245–253.

7 E. V. Pashkova, E. D. Solovyova, T. V. Kolodiazhnyi, V. P. Ivanitskii and A. G. Belous, *J. Magn. Magn. Mater.*, 2014, **368**, 1–7.

8 A. M. Alsmadi, I. Bsoul, S. H. Mahmood, G. Alnawashi, K. Prokes, K. Siemensmeyer, B. Klemke and H. Nakotte, *J. Appl. Phys.*, 2013, **114**, 243910.

9 Z. Mosleh, P. Kameli, A. Poorbaferani, M. Ranjbar and H. Salamati, *J. Magn. Magn. Mater.*, 2016, **397**, 101–107.

10 H. Zhang, J. Li, H. Su, T. Zhou, Y. Long and Z. Zheng, *Chin. Phys. B*, 2013, **22**, 117504.

11 Q. Yang, H. Zhang, Y. Liu and Q. Wen, *Mater. Lett.*, 2009, **63**, 406–408.

12 R. C. Pullar, S. G. Appleton and A. K. Bhattacharya, *J. Magn. Magn. Mater.*, 1998, **186**, 326–332.

13 A. Baykal, I. A. Auwal, S. Güner and H. Sözeri, *J. Magn. Magn. Mater.*, 2017, **430**, 29–35.

14 S. Verma, O. P. Pandey, A. Paesano and P. Sharma, *Phys. B*, 2014, **448**, 57–59.

15 V. C. Chavan, S. E. Shirsath, M. L. Mane, R. H. Kadam and S. S. More, *J. Magn. Magn. Mater.*, 2016, **398**, 32–37.

16 Y. Liu, M. G. B. Drew, J. Wang, M. Zhang and Y. Liu, *J. Magn. Magn. Mater.*, 2010, **322**, 366–374.

17 D. A. Vinnik, D. A. Zherebtsov, L. S. Mashkovtseva, S. Nemrava, M. Bischoff, N. S. Perov, A. S. Semisalova, I. V. Krivtsov, L. I. Isaenko, G. G. Mikhailov and R. Niewa, *J. Alloys Compd.*, 2014, **615**, 1043–1046.

18 D. A. Vinnik, D. A. Zherebtsov, L. S. Mashkovtseva, S. Nemrava, A. K. Yakushechkina, A. S. Semisalova, S. A. Gudkova, A. N. Anikeev, N. S. Perov, L. I. Isaenko and R. Niewa, *Mater. Chem. Phys.*, 2015, **155**, 99–103.

19 C. S. Wang, F. L. Wei, M. Lu, D. H. Han and Z. Yang, *J. Magn. Magn. Mater.*, 1998, **183**, 241–246.

20 L. Wang, H. Yu, X. Ren and G. Xu, *J. Alloys Compd.*, 2014, **588**, 212–216.

21 N. Chen, K. Yang and M. Gu, *J. Alloys Compd.*, 2010, **490**, 609–612.

22 J. Li, H. Zhang, V. G. Harris, Y. Liao and Y. Liu, *J. Alloys Compd.*, 2015, **649**, 782–787.

23 C. Singh, S. Bindra Narang, I. S. Hudiara, Y. Bai and F. Tabatabaei, *Mater. Res. Bull.*, 2008, **43**, 176–184.

24 M. L. Néel, *Ann. Phys.*, 1948, **12**, 137–198.

25 J. Li, H. Zhang, Y. Li, Q. Li and G. Yu, *J. Supercond. Novel Magn.*, 2014, **27**, 793–797.

26 P. Sharma, R. A. Rocha, S. N. Medeiros, B. Hallouche and A. Paesano, *J. Magn. Magn. Mater.*, 2007, **316**, 29–33.

27 A. Ghasemi and A. Morisako, *J. Alloys Compd.*, 2008, **456**, 485–491.

28 S. Ounnunkad, P. Winotai and S. Phanichphant, *J. Electroceram.*, 2006, **16**, 357–361.

29 X. Z. Zhou, A. H. Morrish, Z. Yang and H. X. Zeng, *J. Appl. Phys.*, 1994, **75**, 5556–5558.

30 Z. Zheng and H. Zhang, *IEEE Trans. Magn.*, 2013, **49**, 4230–4233.

31 S. M. Abbas, A. K. Dixit, R. Chatterjee and T. C. Goel, *J. Magn. Magn. Mater.*, 2007, **309**, 20–24.

32 C. G. Koops, *Phys. Rev.*, 1951, **83**, 121–124.

33 X. G. Liu, B. Li, D. Y. Geng, W. B. Cui, F. Yang, Z. G. Xie, D. J. Kang and Z. D. Zhang, *Carbon*, 2009, **47**, 470–474.

34 L. T. Yan, X. J. Wei and G. Z. Kang, *Ferro-Alloys*, 2010, **28**, 5.

35 C. Dong, X. Wang, P. Zhou, T. Liu, J. Xie and L. Deng, *J. Magn. Magn. Mater.*, 2014, **354**, 340–344.

36 S. Ozah and N. S. Bhattacharyya, *J. Magn. Magn. Mater.*, 2013, **342**, 92–99.

37 C. Li, B. Wang and J. Wang, *J. Magn. Magn. Mater.*, 2012, **324**, 1305–1311.

38 N. Chen, K. Yang and M. Gu, *J. Alloys Compd.*, 2010, **490**, 609–612.

39 Y. Wu, Z. W. Li, L. Chen, S. J. Wang and C. K. Ong, *J. Appl. Phys.*, 2004, **95**, 4235–4239.